

## Research Article

# Exploration of Mechanical Behaviors of Argillaceous Siltstone through Photoelastic Model Test and DEM Modelling

Weike Li,<sup>1,2</sup> Jianqiang Han,<sup>2</sup> Jie Cui,<sup>1</sup> Weili Luo ,<sup>1</sup> and Guangzao Zheng<sup>1</sup>

<sup>1</sup>School of Civil Engineering, Guangzhou University, Guangzhou 510006, China

<sup>2</sup>Guangzhou Design Institute, Guangzhou 510620, China

Correspondence should be addressed to Weili Luo; [wlluo@gzhu.edu.cn](mailto:wlluo@gzhu.edu.cn)

Received 12 November 2018; Revised 14 January 2019; Accepted 4 February 2019; Published 4 March 2019

Academic Editor: Sanjay Nimbalkar

Copyright © 2019 Weike Li et al. This is an open access article distributed under the Creative Commons Attribution License, which permits unrestricted use, distribution, and reproduction in any medium, provided the original work is properly cited.

This paper aims at investigating mechanical behaviors of argillaceous siltstone through a photoelastic model test and DEM modelling. Both bonded and unbonded conditions were considered. The photoelastic model was fabricated in a controllable environment, and its scaled factor was 1 : 200 in length and 11.9 : 1 in Young's modulus. The polariscope was designed to have an area-based LCD source and an automatic digital camera. A calibration test was carried out to obtain the relationship between the contact force and the average intensity gradient squared. A 2D DEM simulation is carried out for a 100 mm × 200 mm rectangular container filled with particles of 6 mm and 10 mm, in which the bonding effect is realized by adjusting the shear contact stiffness. The results show that both the photoelastic model and DEM modelling are able to capture the evolution of force chain network, effective contact number and stress concentration factor, and rheological behaviors when it is subjected to an increasing uniaxial load. The bonding effect plays an important role in the mechanical performance of argillaceous siltstone.

## 1. Introduction

Argillaceous siltstone is commonly known as 'problematic rock' in the geotechnical engineering [1–3] because it poses water-softening properties in a way that its strength is significantly reduced upon encountering water. It is now recognized that the properties are caused by interskeleton clay materials that are particularly rich in clay-like components such as kaolinite and illite. Figure 1 provides a scanning electron micrograph of a sample of argillaceous siltstone collected in a building site of Guangzhou (China), in which interskeleton clay materials (grey color) surround skeletons (white color) and serve as bonding cement linking skeletons as a whole to resist external loading. This structure plays an important role in the macroscopic stress-strain relationship and material strength of argillaceous siltstone. Therefore, it is of importance to consider the bonding effect in establishing the relationship between microstructure of the argillaceous siltstone and its macroscopic properties.

During the past few decades, two main approaches have been frequently used to attempt to link the microscopic

structure of soils or rocks with their macroscopic behaviors and have their own features:

- (a) Discrete element method (DEM) [2,4–7]: this method is a promising numerical technique for the macroscopic and microscopic investigations on granular materials, which was originally developed by Cundall in 1971 for the analysis of rock mechanics problems and then applied to soils by Cundall and Strack [4]. Unlike the continuum-based numerical techniques such as finite element method, DEM treats the soils or rock as an assembly of interacted particles that are governed by Newton's laws of motion and the contact constitutive law. The calculation cycle of the DEM is a time-stepping algorithm. At each cycle, the calculation sequence is given as follows: (i) the update of interparticle contacts from known particles, (ii) the update of contact forces based on the relative motion between two particles and the contact constitutive model, and (iii) the update of the velocity and position of each particle from the resultant force and moment based

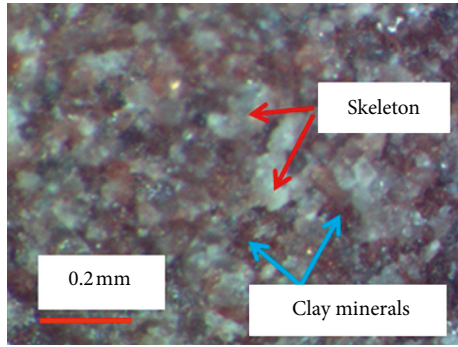


FIGURE 1: Image of a typical argillaceous siltstone in Guangzhou.

on Newton's law of motion. In the literature, the DEM has been successfully employed as a microscopic viewpoint to examine the macroscopic mechanical behavior of granular materials. For example, Jiang et al. [5] simulated the bonding effect of rock and their variations of yielding and bulk modulus against bonding strength or material density by DEM. Zhang et al. [6] carried out the DEM simulations for investigating inherent anisotropy and stress-induced anisotropy of sandy material; Wang et al. [7] simulated the virtual uniaxial compressive tests of AC-16 and predicted its dynamic modulus at different loading frequencies. Molladavoodi and RahimiRezaei [2] successfully simulated the mechanical behaviors of rock and reproduced the experimental stress-strain curve.

- (b) Photoelastic experiments [8–17]: such experiments have been widely undertaken for a variety of stress analysis of an optical material under mechanic deformation since the discovery of the birefringent phenomenon of the optical material in 1816. Most of early applications of the experiments focused on stress analysis of a continuous specimen such as an individual disc made of optical materials. Starting from 1970s, many researchers employed the experiments for investigating the mechanical behavior of an assembly of discs constituting a two-dimensional analogue of a granular material. Drescher and Jong [8] and Drescher [9] performed a test on an assembly of optically sensitive discs of different sizes in order to verify existing flow rules for granular materials, in which their main features such as the subdivision of the assembly into sliding elements and a free rotation of the elements were well observed. Similar tests have been carried out for experimental micromechanical evaluation of other phenomena of granular materials, such as particle rolling [10], interior stress fields of constantly squeezed O-Ring modelling [11], wound closure stresses in sutures [12], force network evolution [11,13], stress-induced anisotropy [14], and jamming transitions [15,16]. Mirbagheri et al. [17] presented a method for measuring forces in granular media experiments using three-dimensional photoelastic gelatin spheres. In comparison with the

two-dimensional discs, the spheres are more flexible and photoelastically sensitive, and thus are more suitable for the use with organisms. Baig et al. [18] carried out a quantitative digital photoelastic analysis on a model of a dry masonry wall with bricks made up of epoxy and found that the force transmission through the wall occurred at discrete points with a tree-like hierarchical pattern of stress flow.

The aforementioned approaches have offered means to interpret macroscopic behavior of a material using its microscopic structure. However, these two approaches have seldom been adopted to investigate the mechanic behaviors of argillaceous siltstone. This paper attempts to explore mechanical behaviors of argillaceous siltstone through a photoelastic model test and DEM modelling. The prototype model of argillaceous siltstone is shown in Figure 1. Both bonded and unbonded conditions are considered. The results are compared between the two groups and are presented in terms of the evolution of force chain network, efficient contact number and stress concentration factor, and rheological behaviors.

## 2. Photoelastic Model Test

*2.1. Experimental Setup.* Figure 2 shows a polariscope for the photoelastic model test of argillaceous siltstone, which was redesigned based on the original polariscope model 409-2 type (manufactured by Beijing Scientific Instrument Limited in the 1980s). The original monochromatic light was replaced by an area-based LCD source, and the latter is more suitable for a photoelastic model of larger size. A loading system was specifically designed such that a uniform compression is applied on the specimen, which consists of a steel frame, a 1:8 steel lever, and a few weights. The specimen was loaded in a rectangular container with the dimension of 100 mm width, 200 mm height, and 3 mm thickness. The top side of the container was under compression, and the other sides were rigidly fixed to the steel frame. The original glass observer was replaced by a digital camera such that the resulting birefringent patterns can be automatically captured.

The working principle of the polariscope is given as follows: (a) the LCD light successively transmits into the first polarizer and the first 1/4 wave plate and becomes linearly polarized and circularly polarized, respectively; (b) the circularly polarized light passes to the specimen under test and thus carries information related to the principal strain/principal stress difference field; (c) the circularly polarized light transmits the second 1/4 wave plate to convert the circular polarization state back to the linear one; (d) the linear polarized light passes the second polarizer that behaves as an analyser; and (e) the camera records the final birefringent patterns.

The experimental model consisted of a series of discs with diameters of 6 mm and 10 mm. The disks were made of epoxy resin because it poses birefringence under a stressed state. The prototype of the model is the argillaceous siltstone

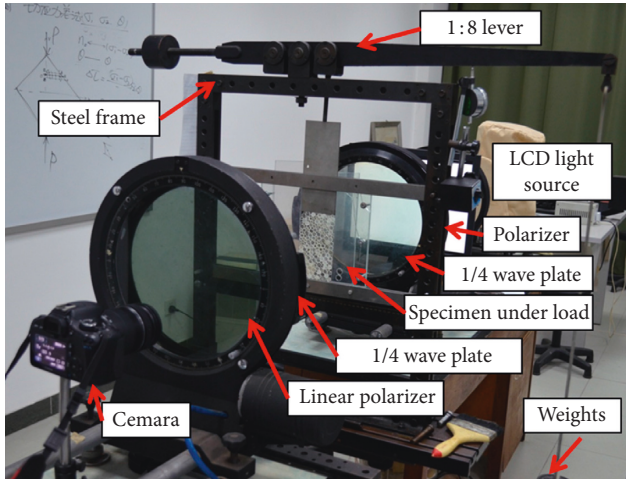


FIGURE 2: Schematic of polariscope.

(Figure 1), containing 72.44% skeleton, 18.80% clay mineral, and 8.76% void. Apart from epoxy, two chemical additives (maleic anhydride and dimethylaniline) were used as a hardening agent and a catalytic agent, respectively. An orthogonal test was carried out to determine the content ratio of epoxy, maleic anhydride, and dimethylaniline in such a way that the resulting epoxy disc has the highest Young's modulus and has a comparable Poisson's ratio as the prototype. The results of the orthogonal test confirmed that the suitable content ratio of epoxy, maleic anhydride, and dimethylaniline is 100 : 32 : 0.2. A standard material test indicated that the resulting epoxy mix has Young' modulus of 4.2 GPa and Poisson's ratio of 0.2.

Figure 3 shows a flow chart of the model fabrication. A 200 mm × 100 mm mold (Figure 4(a)) was first prepared, which was made of glass and strengthened by L-shaped steel frame and nut bolts. The mold was immersed into a release agent made from polystyrene and methylbenzene with a content ratio of 100 : 8, as shown in Figure 4(b). Later, the mold was filled with the mix of epoxy resin, maleic anhydride, and dimethylaniline (Figure 4(c)) and was then placed in a constant temperature oven (54°C) for 72 h. This process is called the first curing, and the liquid form of mix became a hardened plate. After demolding, the plate was immersed into a vessel that was filled with glycerol for 24 h until the second curing was completed. The plate was later cut into 312 discs, including 168 discs with the diameter of 6 mm and 144 discs with the diameter of 10 mm (the ratio between the two is about 1.2 : 1). Finally, the discs were all annealed up to 115°C such that residual stresses caused by the fabrication were eliminated.

In order to model the bonded behavior of clay minerals, silica gel was melted and used as an adhesive gluing one disc to another. The material properties of the adhesive are temperature-sensitive. Figure 5 shows a declined trend of Young's modulus of the adhesive with the increasing temperature. As the experiment was carried out at room temperature of 18°C, Young's modulus of the adhesive was 0.53 GPa, and Poisson's ratio was 0.28.

In summary, Table 1 shows the scaled factors of the skeletons and clay materials.

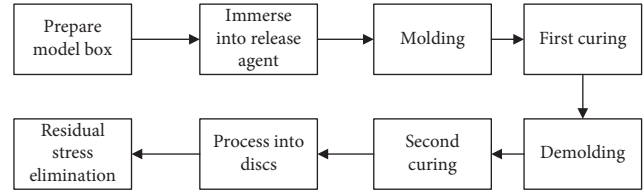


FIGURE 3: Flow chart of the model fabrication.

The fabricated discs were filled into the test container. Two types of condition were considered: one is without adhesive and the other has adhesive among discs to model the bonding effect of clay materials. The void ratio was kept constant and equalled the one of the prototype argillaceous siltstones (8.76%). The void was later filled with glycerol in order to eliminate the effect of the gravity force. The weight was added subsequently, ranging from 0.5 kg to 3 kg with a step of 0.5 kg. This resulted in the compressional force added at the top of container, as shown in Figure 6. It is noted that the steel lever has a scale of 1 : 8.

**2.2. Calibrations and Image Processing.** A calibration test was carried out to establish a direct correlation between the contact force and the amount of birefringent signal. The contact force was applied by a standard material test machine (MTS), ranging from 5 N to 100 N with a load step of 5 N. The amount of birefringent signal was characterized by the average intensity gradient squared ( $G^2$ ) [19]:

$$G^2 = \frac{1}{N} \sum \nabla I_{x,y}^2, \quad (1)$$

where  $\nabla I_{x,y}^2$  is a four-way average of the intensity difference squared divided by the distance and  $N$  is the number of pixels of the birefringent image.

In this paper, the value of  $G^2$  is calibrated to the forces of two groups of discs (10 mm and 6 mm). As shown in Figure 7, the value of  $G^2$  is almost a linear function of the applied force  $F$  when the force is less than 40 N. Above 40 N, the linear relationship is compromised. Consequently, a polynomial function with the order of three was used to fit experimental results, and the confidence level is larger than 99%, which is given in the legend of Figure 7. Once the average intensity gradient squared  $G^2$  of is determined, the value of the applied force  $F$  is obtained by seeking the positive root of the polynomial function.

The digital camera was set to be automatic, capturing birefringent images every 10 s. The distance between the camera and the polariscope is the same as that in the calibrated test, ensuring the validity of the fitted formula in Figure 7. The image was processed using a self-developed program in Matlab. Main procedures are given as follows: (a) converting the original image into binary one, (b) identifying the center and the radius of each disc, (c) calculating the contact force between two discs based on the relationship between the average intensity gradient squared and the applied force, and (d) visualizing the identified force chain.

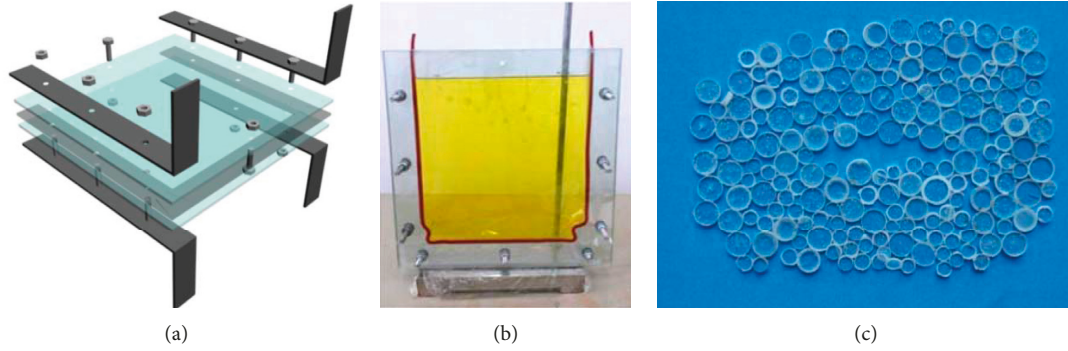


FIGURE 4: Experimental setup for the model fabrication. (a) Mold. (b) Molding. (c) Discs.

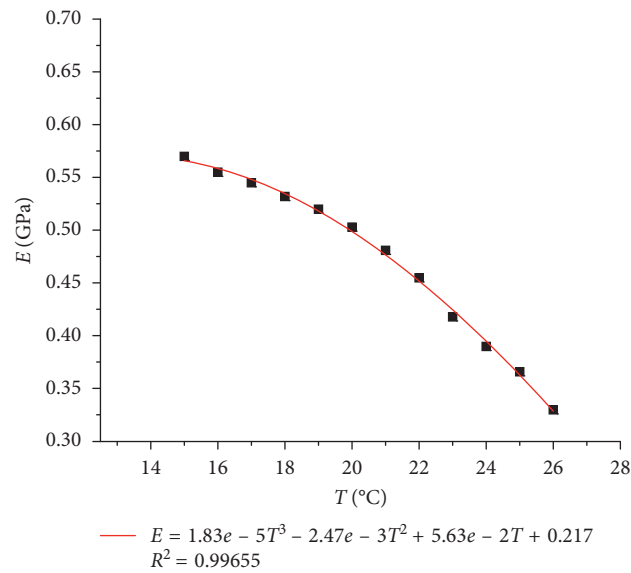


FIGURE 5: Relationship between Young's modulus of the adhesive and temperature.

TABLE 1: Model parameters.

Parameters	Dimension	Scaled factor (prototype/model)	Prototype	Model
Diameter of skeleton	$L$	1 : 200	0.03 mm/0.05 mm	6 mm/10 mm
Young's modulus of skeleton	$M/(L * T^2)$	11.9 : 1	50 GPa	4.2 GPa
Poisson's ratio of skeleton	—	1 : 1	0.15~0.22	0.20
Young's modulus of clay mineral	$M/(L * T^2)$	11.9 : 1	6.2 Gpa	0.53 GPa*
Poisson's ratio of clay mineral	—	1 : 1	0.25	0.28*

\*Measurement at room temperature of 18°C.

### 2.3. Experimental Results

**2.3.1. Force Chain Network.** Interparticle forces are transmitted from one particle to the next via their contacts, which are commonly depicted by a force chain network. In this work, the force chain network is characterized by the force chain distribution and the force angle distribution. The former shows the location of the interparticle forces, and the latter gives a statistical index indicating the proportion of the interforces' angles. In the following paragraphs, results are shown for both unbonded and bonded discs.

Table 2 lists the distribution of force chain and force angle for unbonded discs when they are subjected to a lever

weight ranging from 0.5 kg to 3 kg. When the lever weight is 0.5 kg, only a small portion of discs are active and the force chain only involves a few discs. The force angles are mainly distributed within  $30^\circ$  with respect to the horizontal line and the vertical line, corresponding to the internal friction angle of the discs. As the lever weight continues to increase, more and more force chains appear and they interconnect more discs together to resist external loading. It is noted that the force chains at a lower lever weight do not necessarily exist in the case at a higher lever weight, and they work in a way that they are naturally optimized to match the external loading. Meanwhile, the force angle varies dramatically as the lever weight increases. The force chains with force angles less than

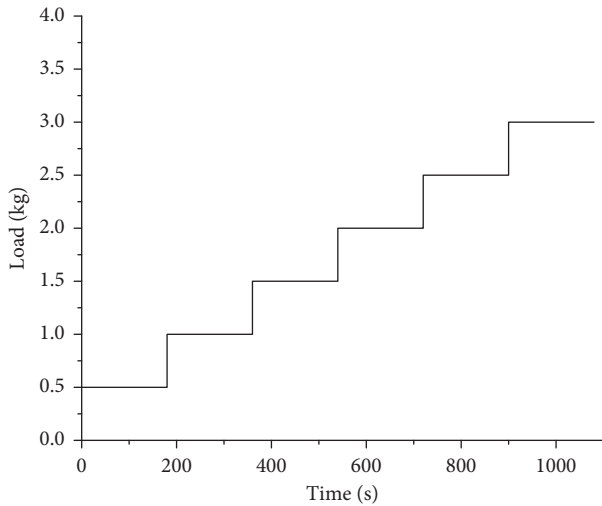


FIGURE 6: Loading curve.

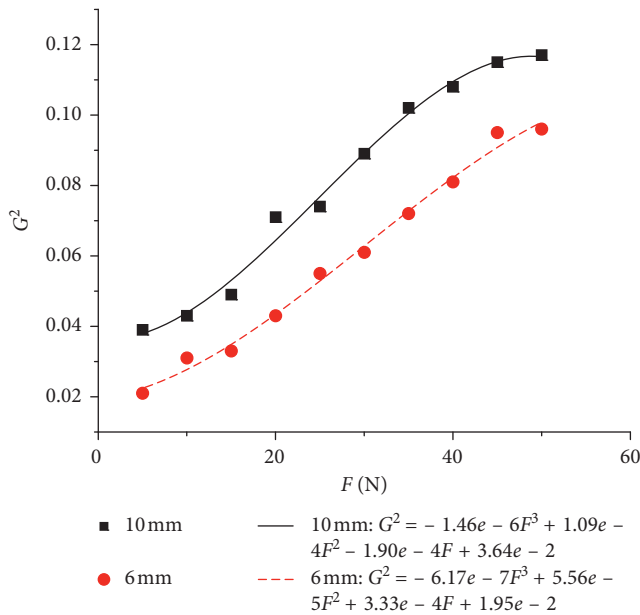


FIGURE 7: Correlation of applied force  $F$  to the value of  $G^2$ .

30° always have the highest probability density, regardless of the lever weight. This is due to the fact that the effect of internal friction is the sole contribution to shear strength of the unbonded discs.

As a comparison, Table 3 lists the distribution of force chain and force angle for bonded discs when they are subsequently subjected to the same lever weights as the unbonded case. When the bonding effect is taken into consideration, a quite significant increase is observed in both the amounts of active discs and force chains, regardless of lever weights. This is because the adhesive ties all discs as a whole such that more particles would respond during external loading. As the lever weight increases, the bonded discs pose similar trends in the force chain distribution as the unbonded ones: more discs become active and the force chains are more and longer. For the force angle distribution,

the main angle is within 30° when the lever weight is relatively low (taken the cases of 0.5, 1, and 1.5 kg, for example). This is similar to the unbonded case, implying that the effect of internal friction plays a more important role than the bonding effect in the case with relatively low loads. As the lever weight continues to increase, the force angle distributes more evenly. For instance, the force chains at the lever weight of 3 kg nearly have angles evenly distributed in a range of  $[0, 2\pi]$ . This is because the bonding effect acts as an increasingly important role in the shear strength of bonded discs. It is worth mentioning that the bonded strength of the adhesive is not exceeded in the test and the bonded discs are intact after the test.

2.3.2. *Evidences of Rheological Behaviors.* Rheological properties are one of the typical features of argillaceous siltstone, which are characterized by macroscopic behaviors such as creep and relaxation. The photoelastic model in this paper allows the observation of creep because each step of load has been applied constantly for 200 s such that the resultant stress can be regarded to be uniform during each loading. An example is shown in Figure 8 when the bonded discs are subjected to the load weight of 0.5 kg. In the comparison between the image at 10 s (Figure 8(a)) and the image at 20 s (Figure 8(b)), only a few discs undergo a bit change in stress while the stress state of the rest of the discs is almost the same. An evidence of the change can be further identified in Figure 8(c) by subtracting the figure at 20 s (Figure 8(b)) from the figure at 10 s (Figure 8(a)). This suggests that the macroscopic rheological behaviors of argillaceous siltstone are realized by a little adjustment of stress state in a few discs in a way that a more efficient force chain is formed to resist external loading.

The rheological behaviors can be also quantified by the vertical strain of the specimens, which is defined to be a ratio of vertical displacement of the sample to its original height. Figure 9 shows the vertical strain time history of the bonded and unbonded discs. It can be observed that, at each step of loading, the strain increases quite dramatically for the first 100 s and then tends to be constant for the second 100 s. As a result of bonded effect of clay materials, the bonded specimen undergoes lower levels of strain than the unbonded one. The strain increases with the increase of applied load.

In order to better describe the rheological behavior of the specimens, an index of rheological strain is introduced, which is defined as the subtraction of the initial strain at each step of loading from the maximal strain at the end of the step. Figure 10 compares the rheological strain between the bonded and unbonded specimens. The rheological deformation of unbonded discs decreases at first and then increases as the load continues to increase. This can be interpreted that the unbonded discs firstly undergo compaction and become denser under the increasing load, and then interparticle slippages are believed to occur as the load continues to increase. For the bonded discs, the rheological strain tends to show a general decline trend as the applied load increases. This implies that the bonded discs are in the

TABLE 2: Distribution of force chain and force angle for unbonded particles.

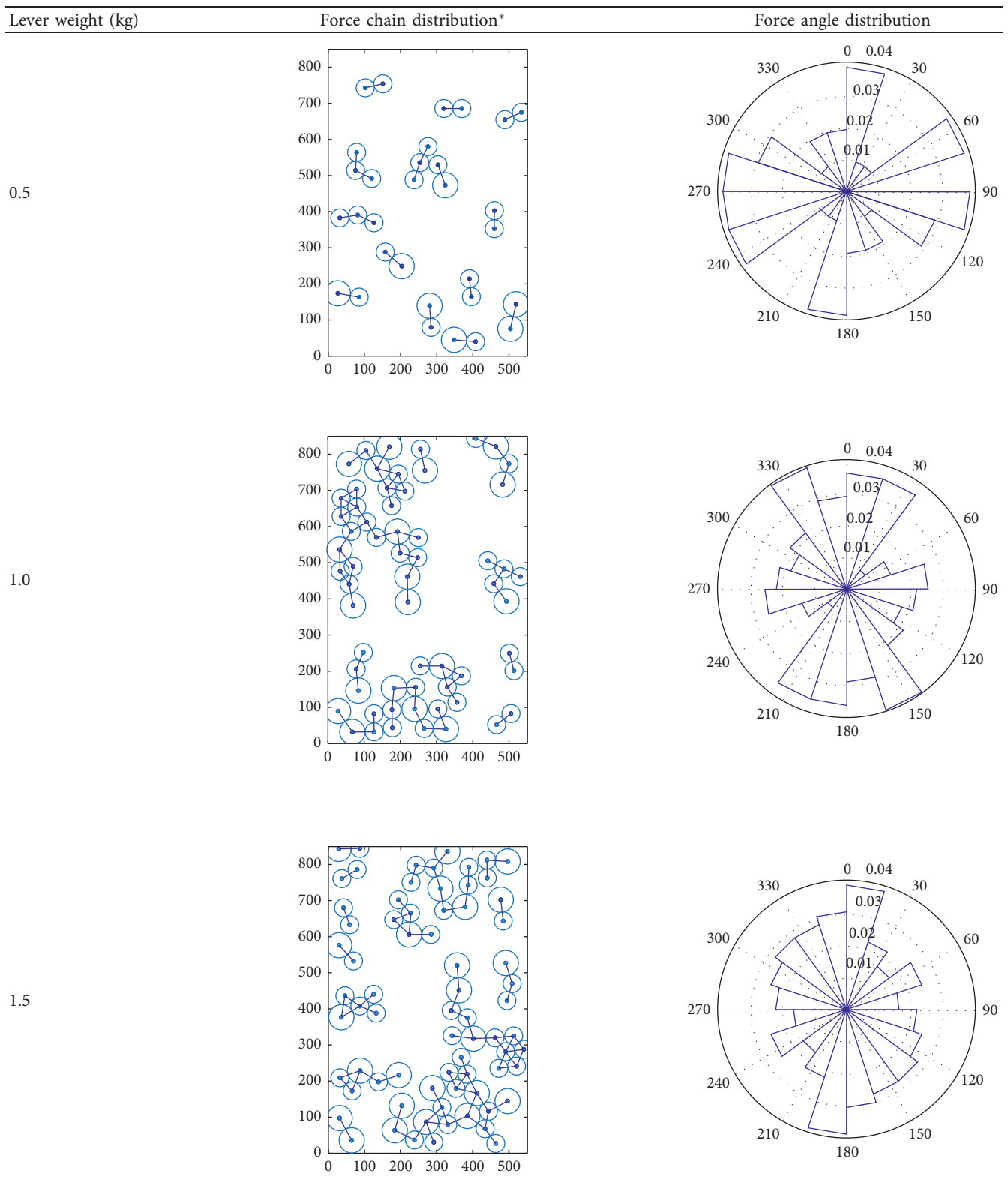
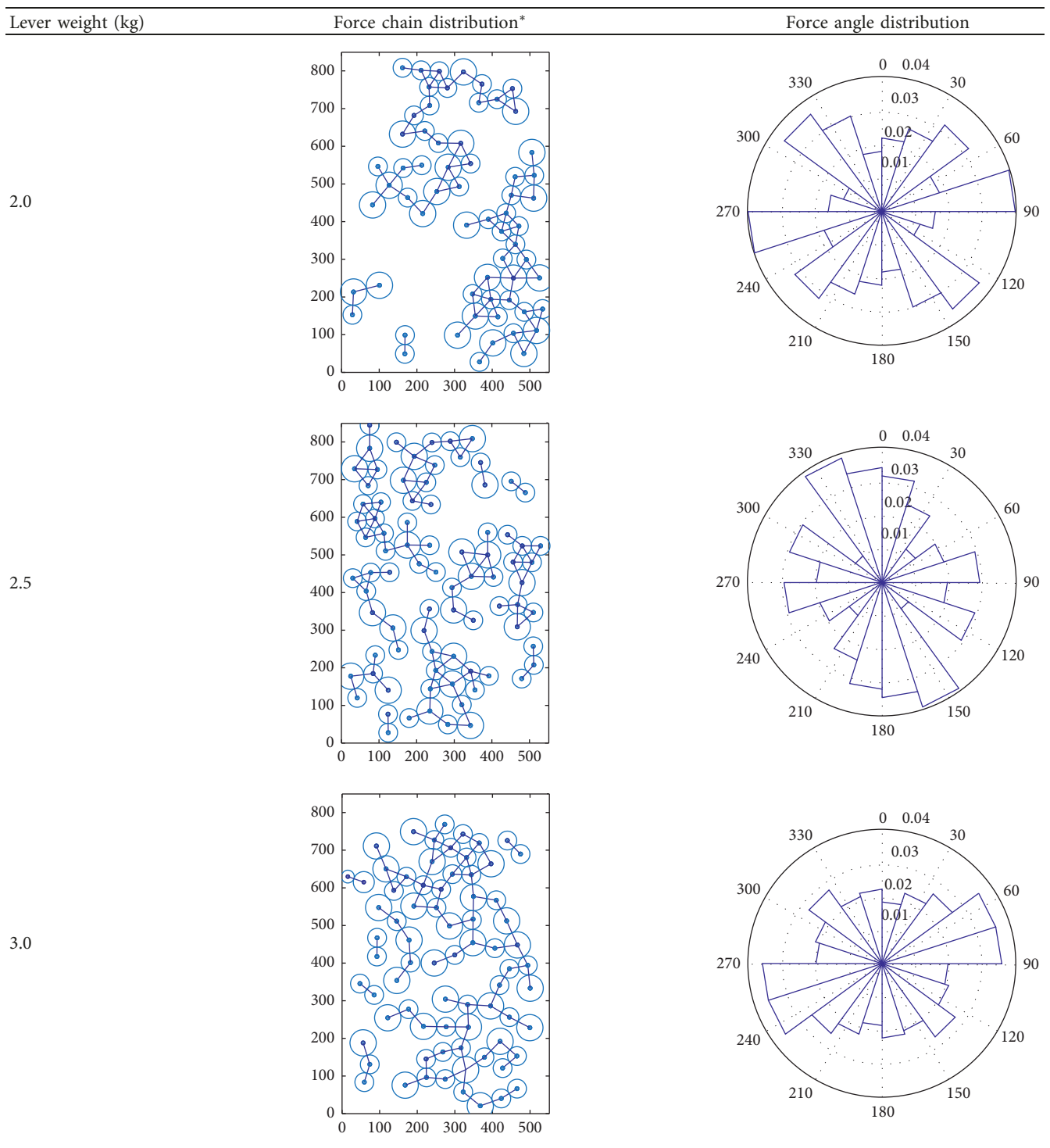


TABLE 2: Continued.



\*Only those force chains having higher than the average value are shown; units of the  $x$ - and  $y$ -axes are pixels.

process of compaction such that the density of the specimen becomes larger.

### 3. DEM Modelling

3.1. Numerical Setup. Figure 11 shows the particle distribution in DEM modelling which is applied in the test to

simulate the photoelastic model test of argillaceous siltstone. The 100 mm × 200 mm rectangular container was evenly filled with particles, including two sizes of 6 mm and 10 mm, respectively. The number and the ratio of two groups of particles are kept the same as those in the photoelastic model test, that is, 168:144 ≈ 1.2:1. Based on DEM modelling fitting on photoelastic experiment, the particle density is

TABLE 3: Distribution of force chain and force angle for bonded particles.

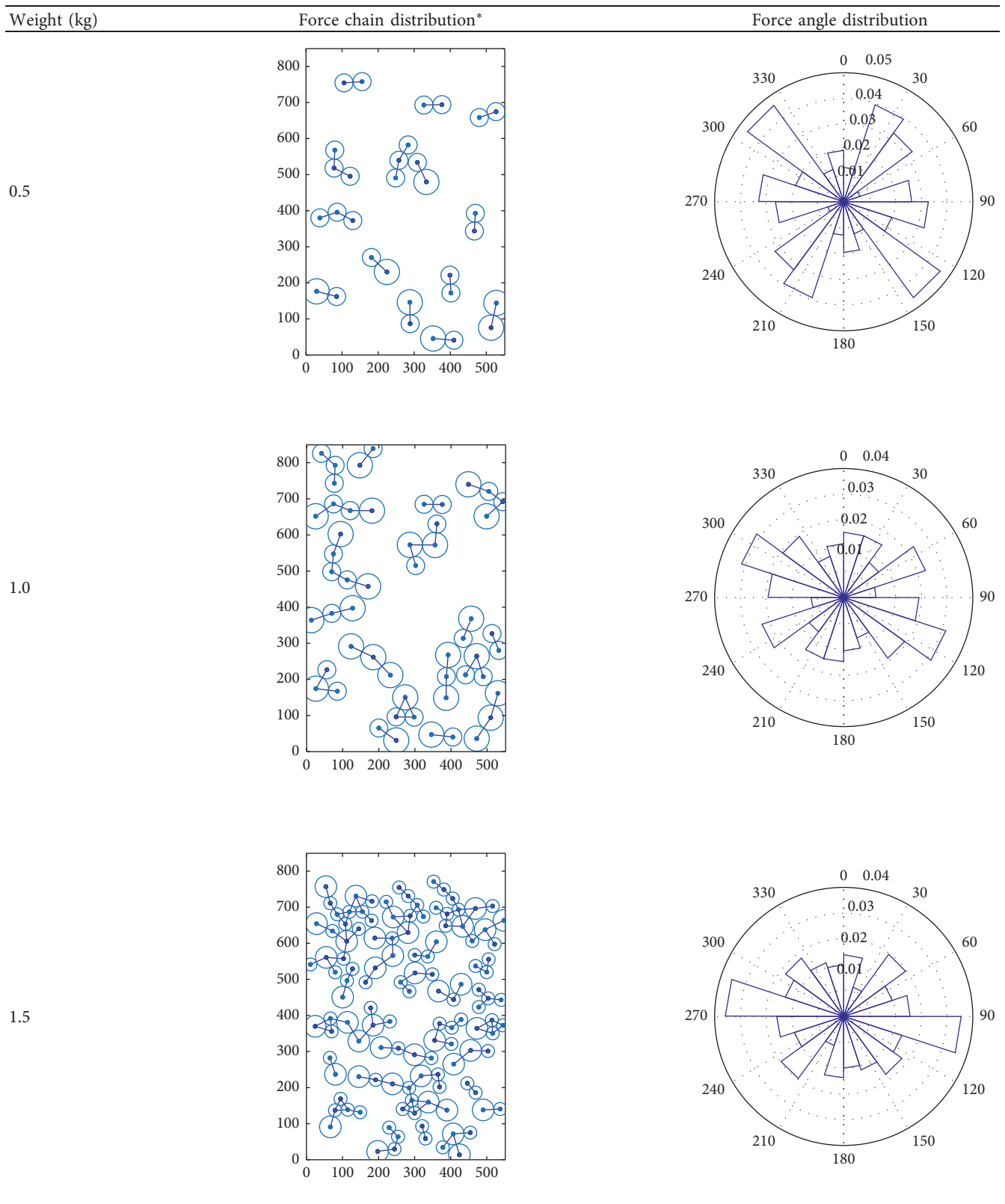
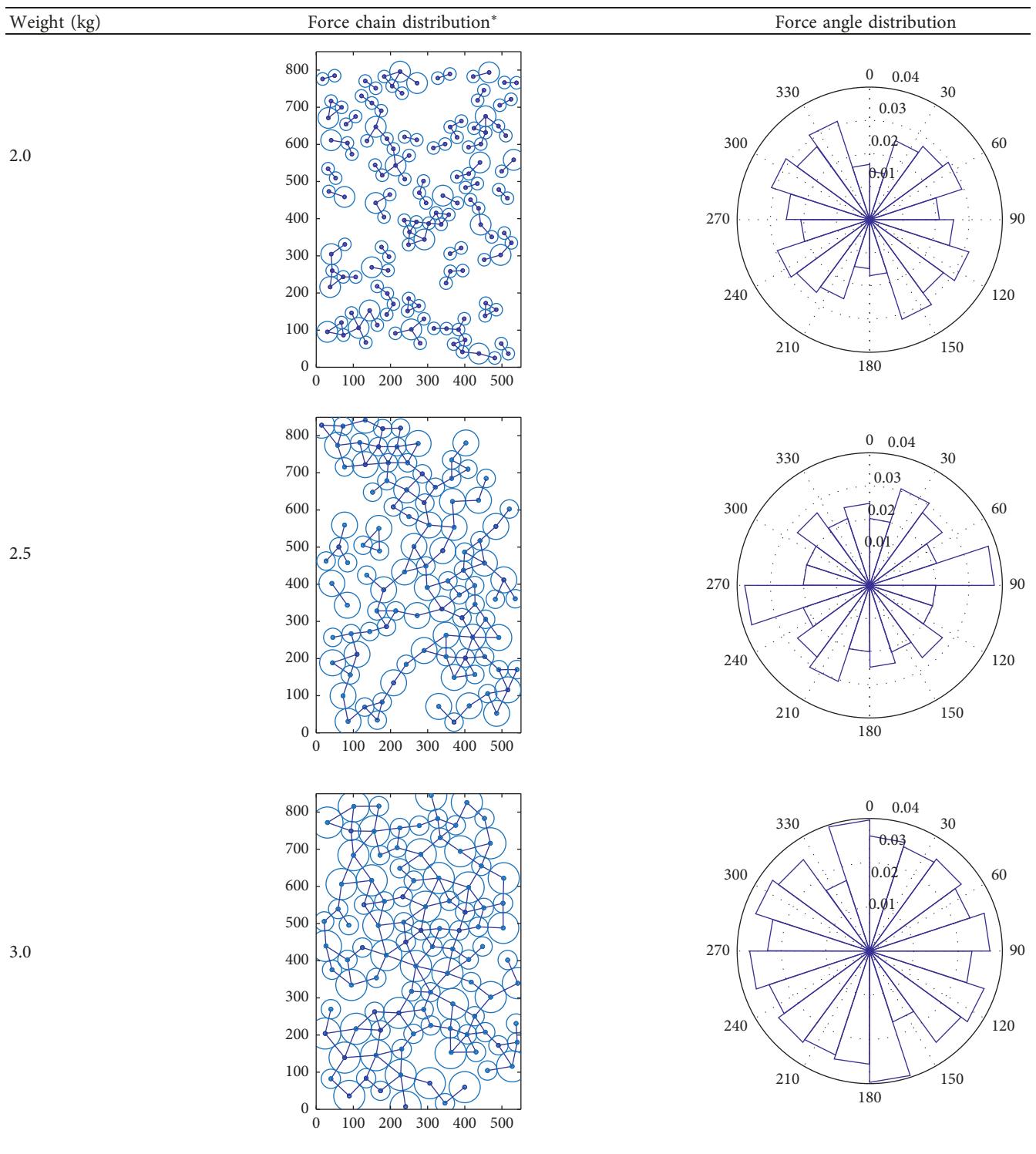


TABLE 3: Continued.



\*Only those force chains having higher than the average value are shown; units of  $x$ - and  $y$ -axes are pixels.

chosen as  $2000 \text{ kg/m}^3$ , and normal contact stiffness and porosity are chosen as  $1e8 \text{ kPa}$  and  $0.168$ . The coefficient of friction between the particles is set to  $0.5774$ , corresponding to the internal friction angle of  $30^\circ$ . The value for the no-tension flag is activated. At each step, the volumetric strain and normal contact force are monitored. The load is

achieved by servocontrol mechanism. Through controlling the moving direction and velocity of top side of the container while setting its rest sides to be rigid, the servocontrol mechanism can maintain the quasistatic pressures on the top. The DEM container finally gets to the quasistatic state with a target load, which is chosen as  $3.5 \text{ MPa}$  for the loaded

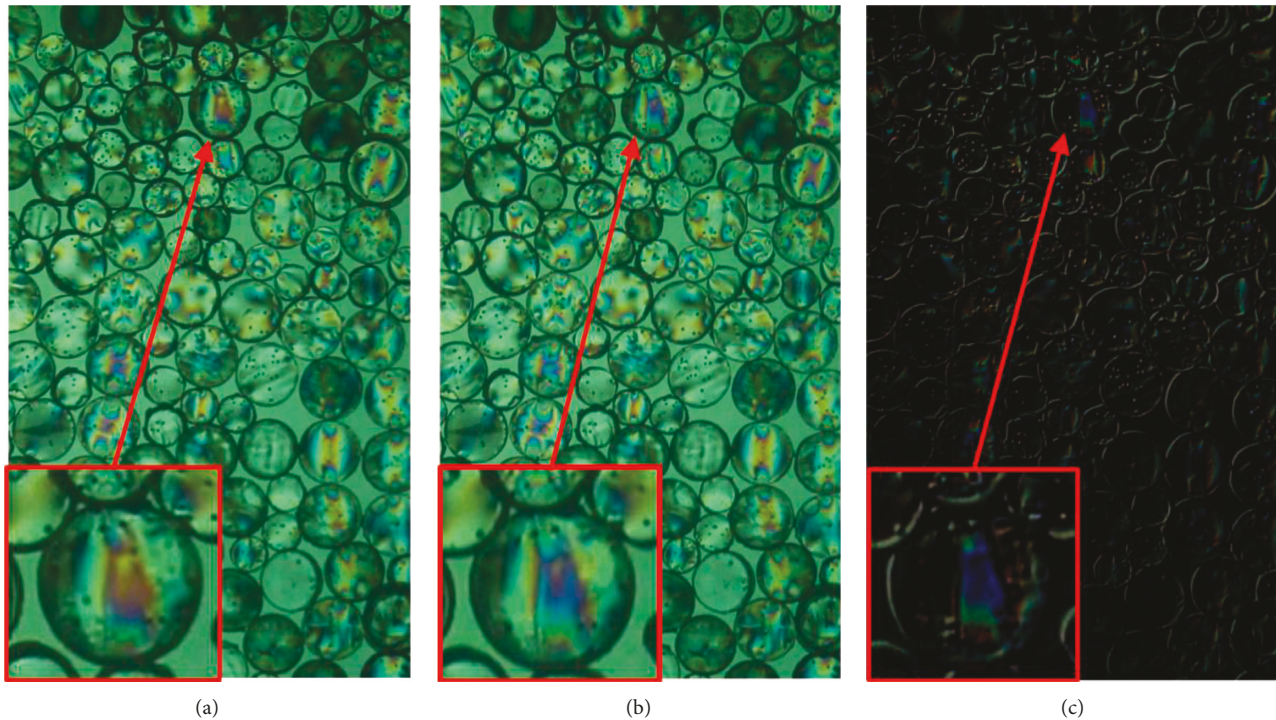


FIGURE 8: An example of rheological behaviors of the bonded particles under the load weight of 0.5 kg: (a) 10 s, (b) 20 s, and (c) the difference between figures at 10 s and 20 s.

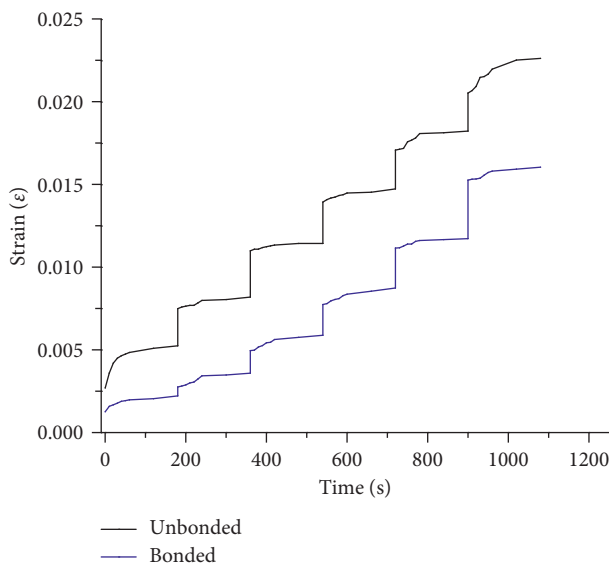


FIGURE 9: Time history of vertical strains of the bonded and unbonded samples.

state in this study. The bonded condition is realized by setting shear contact stiffness among particles, while this value is zero for the unbonded case.

3.2. Numerical Results. DEM modelling results in terms of the distribution of force chain and force angle for unbonded particles are presented in Figure 12(a) when they are applied

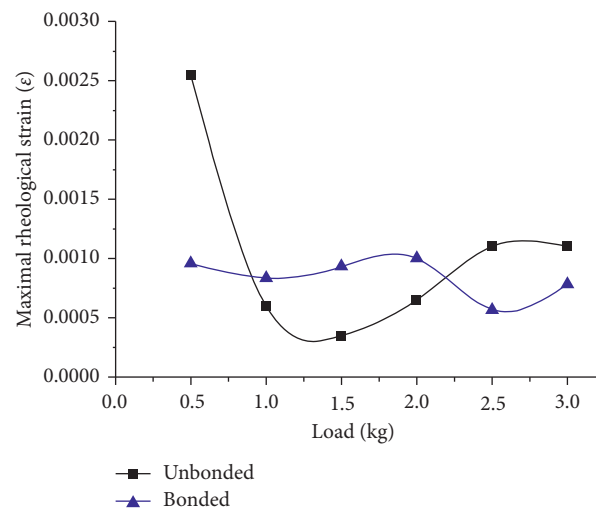


FIGURE 10: Comparison of rheological strain between the bonded and unbonded samples.

with a lever weight of 0.5 kg. It is clearly found that only a few numbers of particles are active and most of force angles are less than  $30^\circ$  with respect to the horizontal line and the vertical line. These phenomena are consistent with the observed results (first row of Table 3) in the photoelastic model test. It should be stressed that the detailed distribution of force chain is not exactly the same because of the randomness in the DEM modelling. As the load increases, as shown in Figure 12(b), more and more force chains appear and the angle of force becomes more and more uniform.

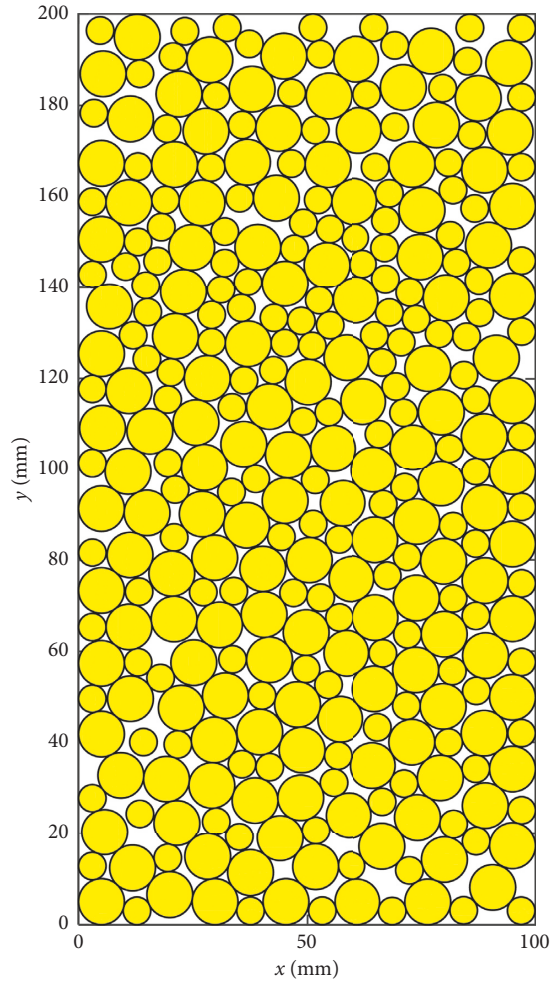


FIGURE 11: Particle distribution in DEM modelling.

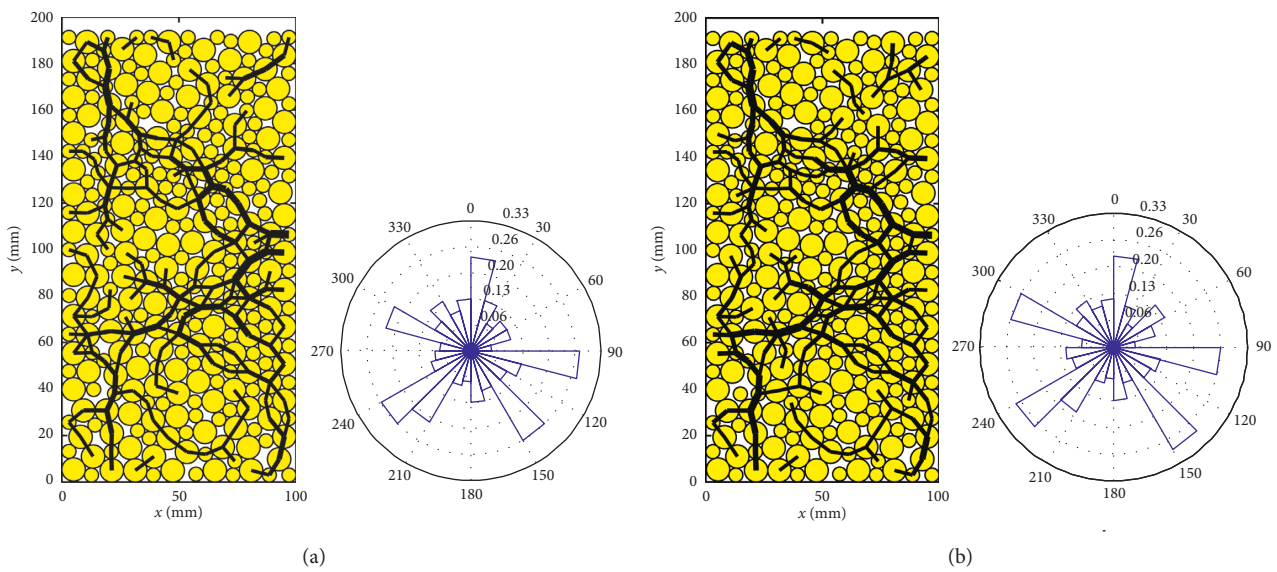


FIGURE 12: Distribution of force chain and force angle for unbonded particles in the DEM modelling, under the lever weights of (a) 0.5 kg and (b) 2.0 kg.

These tendencies are well reproduced by the DEM modelling. Similar conclusions can be obtained for other lever weights, and thus their results are not presented for the sake of brevity.

Figure 13 shows the distribution of force chain and force angle for bonded particles in the DEM modelling. Because of the consideration of bonding effect, more contact force chains appear as compared with the unbonded cases (Figure 12). This suggests that the bonding effect ties all particles as an entirety for resisting external loadings. As the normal force increases, there is a significant increase in the number of unbonded force chains, as shown in Figure 13(b). The experimental results are very close to those of the photoelastic experiment but not exactly same. With the normal load getting larger, it can be seen that the force angle is more evenly distributed. This is because, as mentioned in Section 2.3.1, the bonding effect acts as an increasingly important role in the shear strength of bonded discs.

#### 4. Discussions

This section compares the results of photoelastic model test and DEM modelling and discusses temporal results in terms of the evolution of the strain and two statistical results (the effective contact number and the stress concentration).

**4.1. Evolution of Strain.** Figure 14 shows the evolution of the strain of discs in both the photoelastic model test and DEM modelling when the lever weight subsequently increases from 0.5 kg to 3 kg. In the photoelastic model test, an almost linear curve is observed with respect to the lever weight for both bonded and unbonded cases, confirming that all experimental tests are kept in the linear state. It is expected that the bonded discs as a whole has a higher value in Young's modulus than the unbonded case. This can be confirmed from the strain-loading curve that the bonded case has a lower slope as compared with the unbonded case. As the applied load increases, the strains at both cases increases and the strain value of the bonded case is increasingly higher. This implies that the bonding effect of argillaceous siltstone enhances the interaction among individual particles. These laboratory test results of the unbonded and bonded cases are reasonably predicted by the DEM modelling with shear contact stiffness  $k_s = 0$  and  $1e8$  kPa, respectively. As the value of the shear contact stiffness becomes larger, their curves show a tendency to that of the bonded case.

**4.2. Evolution of Effective Contact Number.** Corresponding to the photoelastic model test, only those force chains having larger values than the mean value of all force chains are recorded as valid force chains in this paper. The number of valid force chain at each disc is the effective contact number at the disc. Thus, the effective contact number for all discs  $c$  is defined as the average number of effective contact number per disc:

$$c = \frac{2B}{N}, \quad (2)$$

where  $B$  is the number of force chains having larger values than the mean value of all force chains and  $N$  is the total number of discs in the captured image.

Figure 15 compares the evolution of effective contact numbers of both bonded and unbonded specimen as a function of the applied loads. For the unbonded case, the effective contact number increases significantly at the beginning (from 0.5 kg to 1.5 kg of load). This is because the increasing load makes the specimen denser in a way that more contacts are active. As the load continues to increase, the effective contact number tends to be steady and then to decrease a bit. In this period, the specimen has sufficient contacts to resist external loading, and the increase of the load is balanced via internal deformations of each disc as well as interparticle frictions. The decrease in the effective contact number is because of the effect of shear dilation of discs. These phenomena are well predicted by DEM, and the error of the DEM modelling is about 3.6%. For the bonded case, the effective contact number increases slowly at first and then quite dramatically as the applied load increases. This is due to the fact that the clay materials (adhesive in this paper) serves as a natural link among discs, and more force chains will be active as the load increases. The above-mentioned phenomena are fairly predicted by the DEM modelling with shear contact stiffness  $k_s = 1e8$  kPa, and the error of the DEM modelling is about 5.2%. As the value of the shear contact stiffness becomes smaller (say  $k_s = 1e6$  kPa and  $k_s = 1e7$  kPa), their curves show a tendency to that of the unbonded case.

**4.3. Evolution of Stress Concentration.** It has been shown in Tables 2 and 3 that the transmission of force among discs is not uniform. This effect is quantified in this paper by a factor of stress concentration ( $\alpha_K$ ), which is defined as follows:

$$\alpha_K = \frac{\sigma_{\max}}{\langle \sigma \rangle}, \quad (3)$$

where  $\sigma_{\max}$  and  $\langle \sigma \rangle$  are the maximum stress and the average stress among all discs, respectively. As the stress in the photoelastic test is directly related to the average intensity gradient squared  $G^2$ , equation (3) becomes

$$\alpha_K = \frac{G_{\max}^2}{\langle G^2 \rangle}, \quad (4)$$

where  $\langle G^2 \rangle$  is the average value of  $G^2$  among all particles.

Figure 16 compares the stress concentration factors between photoelastic model test and DEM modelling when the lever weight subsequently increases from 0.5 kg to 3 kg. Both the bonded and unbonded cases are considered. For the unbonded case, the stress concentration factor shows a general increase trend as the lever weight increases. This is because in the unbonded case most of interparticle forces are not active and the force among discs is generally transmitted via a small portion of discs, as shown in Table 2. For the bonded case, the stress concentration factor is generally lower than that of the unbonded one. This phenomenon is a result of the bonded effect that makes all discs as a whole to resist external loading and transmit forces (Table 3). As the

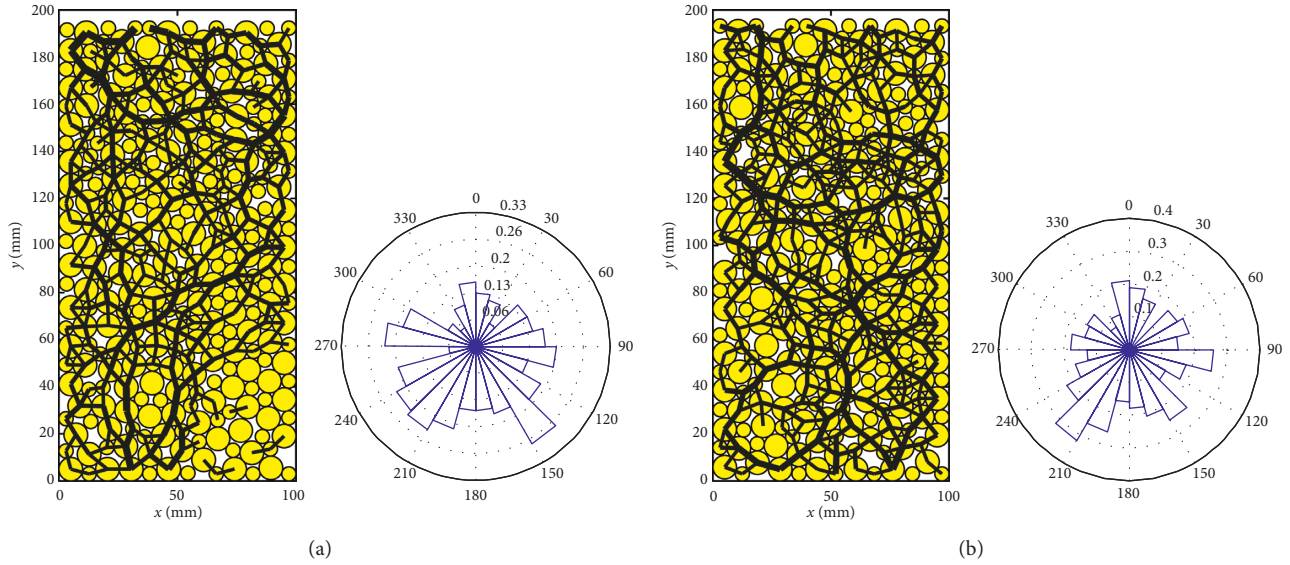


FIGURE 13: Distribution of force chain and force angle for bonded particles in the DEM modelling, under the lever weights of (a) 0.5 kg and (b) 2.0 kg.

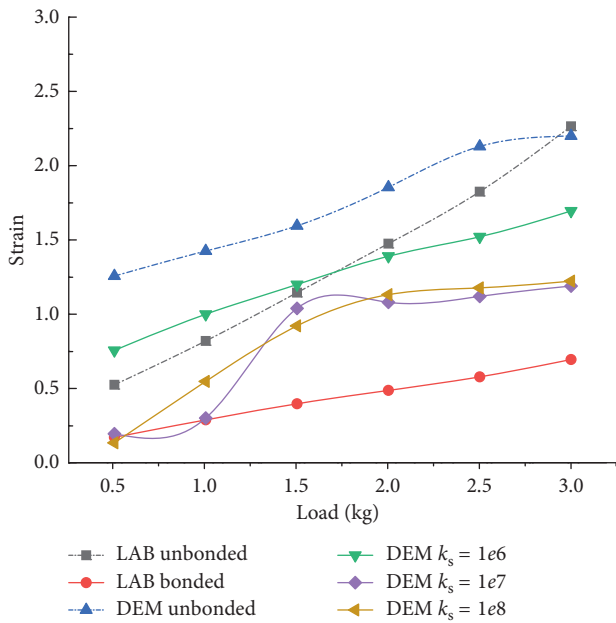


FIGURE 14: Comparison of strain evolution in both the photoelastic mode test and DEM modelling.

lever weight increases, the stress concentration factor increases at first to a certain level and then decreases steadily. It is revealed that the amount of the stress increment is mainly sustained by the skeletons (discs) in the initial stage of loading, and the clay minerals (silica gel as the adhesive in the model) starts to sustain a part of the load as the load increases. Under the later situation, the stress concentration factor of the skeletons no longer increases. This usually results in a shear failure in the clay materials and thus the failure of the argillaceous siltstone. It is noted that the clay materials have weaker strength than the skeletons. The

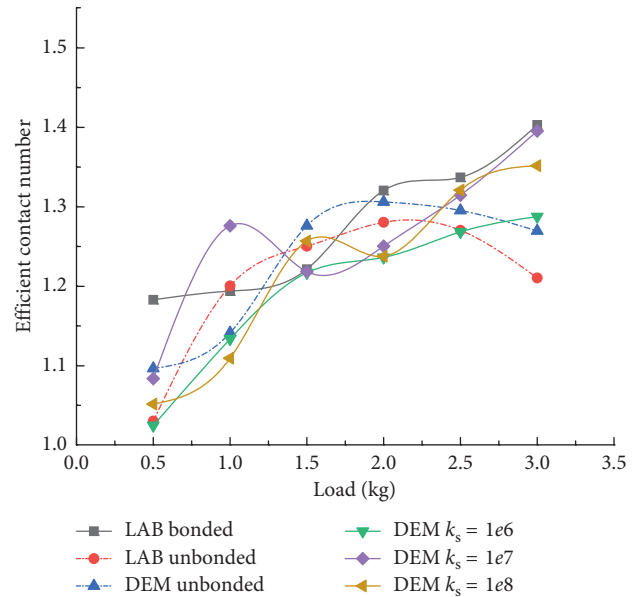


FIGURE 15: Comparison of effective contact numbers between photoelastic mode test and DEM modelling.

abovementioned observations can be also found in the curves of DEM modelling with  $k_s = 1e8$  kPa. A decrease in the shear contact stiffness generally increases the stress concentration factor; meanwhile, the curve becomes steeper. The average errors of the DEM modelling are 4.5% and 5.9% about for the unbonded and bonded cases, respectively.

### 5. Conclusions

Based on a photoelastic model and DEM modelling, the mechanical behaviors of argillaceous siltstone are studied. The evolution of force chain network, effective contact

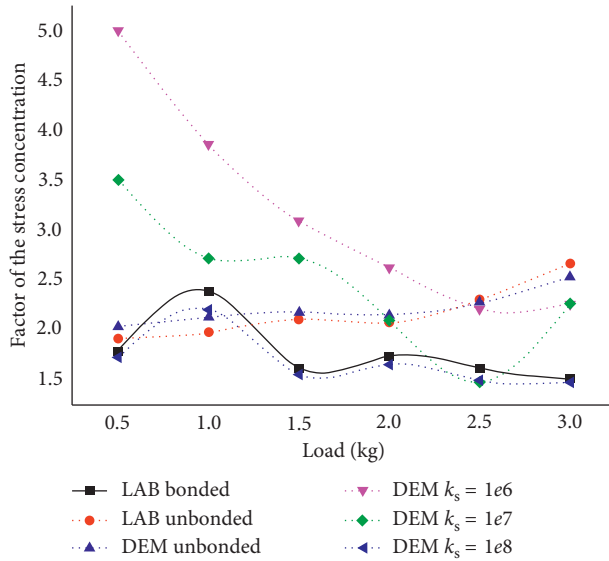


FIGURE 16: Comparison of stress concentration factor between the photoelastic mode test and DEM modelling.

number and stress concentration factor, and rheological behaviors are compared between the models under unbonded and bonded conditions. The following conclusions are drawn:

- (1) Force chain network works in a way that it is naturally optimized to match the external loading. The force chain involves more discs in the bonded case than in the unbonded case because the adhesive in the former ties all discs as a whole such that more discs would respond during external loading. The effect of internal friction always plays a more important role, regardless of the bonding condition. In the bonded case, the bonding effect plays an increasingly important part in the shear strength as the external load increases.
- (2) Quite distinct phenomena are observed in terms of the effective contact number. For the unbonded case, it increases significantly at the beginning and then tends to decrease. For the bonded case, it increases slowly at first and then quite dramatically as the applied load increases.
- (3) As the lever weight increases, the stress concentration factor shows a general increase in the unbonded case, and the factor in the bonded case increases at first to a certain level and then decreases steadily.
- (4) The macroscopic rheological behaviors of argillaceous siltstone are realized through a little adjustment of stress state in a few discs in a way that a more effective force chain network is formed to resist external loading. The bonded specimen undergoes lower levels of strain than the unbonded one. The strain increases with the increase of applied load.

## Data Availability

The data that support the findings of this study are available from the corresponding author upon reasonable request.

## Conflicts of Interest

The authors declare that they have no conflicts of interest.

## Acknowledgments

This research was supported by the National Natural Science Foundation of China (project nos. 51608138 and 41502262) and the National Key Research and Development Program of China (project no. 2016YFC0800205).

## References

- [1] J. Chen, F. Dai, L. Xu et al., "Properties and microstructure of a natural slip zone in loose deposits of red beds, southwestern China," *Engineering Geology*, vol. 183, no. 9, pp. 53–64, 2014.
- [2] H. Molladavoodi and Y. RahimiRezaei, "Heterogeneous rock simulation using DIP-micromechanics-statistical methods," *Advances in Civil Engineering*, vol. 2018, Article ID 7010817, 10 pages, 2018.
- [3] B. Y. Zhang, J. H. Zhang, and G. L. Sun, "Particle breakage of argillaceous siltstone subjected to stresses and weathering," *Engineering Geology*, vol. 137–138, no. 7, pp. 21–28, 2012.
- [4] P. A. Cundall and O. D. L. Strack, "A discrete numerical model for granular assemblies," *Géotechnique*, vol. 29, no. 1, pp. 47–65, 1979.
- [5] M. Jiang, H.-S. Yu, and S. Leroueil, "A simple and efficient approach to capturing bonding effect in naturally micro-structured sands by discrete element method," *International Journal for Numerical Methods in Engineering*, vol. 69, no. 6, pp. 1158–1193, 2007.
- [6] K. Zhang, Z. Zang, L. Okine, and J. L. Chavez Torres, "Microstudy of the anisotropy of sandy material," *Advances in Civil Engineering*, vol. 2018, Article ID 3971643, 13 pages, 2018.
- [7] D. Wang, X. Ding, T. Ma, W. Zhang, and D. Zhang, "Pavement analysis and design by multiphysics reconstructing algorithm for the virtual asphalt mixture based on the discrete-element method," *Advances in Civil Engineering*, vol. 2018, Article ID 5180562, 11 pages, 2018.
- [8] A. Drescher and G. Jong, "Photoelastic verification of a mechanical model for the flow of a granular material," *Journal of the Mechanics and Physics of Solids*, vol. 20, no. 5, pp. 337–340, 1972.
- [9] A. Drescher, "An experimental investigation of flow rules for granular materials using optically sensitive glass particles," *Géotechnique*, vol. 26, no. 4, pp. 591–601, 1976.
- [10] M. Oda, J. Konishi, and S. Nemat-Nasser, "Experimental micromechanical evaluation of strength of granular materials: effects of particle rolling," *Mechanics of Materials*, vol. 1, no. 4, pp. 269–283, 1982.
- [11] D.-C. Shin, J.-H. Nam, and D.-W. Kim, "Experimental interior stress fields of a constantly squeezed O-ring modeling from hybrid transmission photoelasticity," *Experimental Techniques*, vol. 40, no. 1, pp. 59–72, 2016.
- [12] D. Hoy and K. Gingras, "Photoelastic study of wound closure stresses in barbed versus traditional smooth-surface sutures," *Experimental Techniques*, vol. 39, no. 2, pp. 31–37, 2015.
- [13] R. R. Hartley and R. P. Behringer, "Logarithmic rate dependence of force networks in sheared granular materials," *Nature*, vol. 421, no. 6926, pp. 928–931, 2003.
- [14] T. S. Majmudar and R. P. Behringer, "Contact force measurements and stress-induced anisotropy in granular materials," *Nature*, vol. 435, no. 7045, pp. 1079–1082, 2005.

- [15] T. S. Majmudar, M. Sperl, S. Luding, and R. P. Behringer, "Jamming transition in granular systems," *Physical Review Letters*, vol. 98, no. 5, 2007.
- [16] A. Tordesillas, "Force chain buckling, unjamming transitions and shear banding in dense granular assemblies," *Philosophical Magazine*, vol. 87, no. 32, pp. 4987–5016, 2013.
- [17] S. A. Mirbagheri, E. Ceniceros, M. Jabbarzadeh, Z. McCormick, and H. C. Fu, "Sensitively photoelastic bio-compatible gelatin spheres for investigation of locomotion in granular media," *Experimental Mechanics*, vol. 55, no. 2, pp. 427–438, 2015.
- [18] I. Baig, K. Ramesh, and M. P. Hariprasad, "Analysis of stress distribution in dry masonry walls using three fringe photoelasticity," in *Proceedings of 14th International Conference on Experimental Mechanics*, Singapore, November 2014.
- [19] J. Liu, Q. Sun, and F. Jin, "Visualization of force networks in 2D dense granular materials," *Frontiers of Architecture and Civil Engineering in China*, vol. 4, no. 1, pp. 109–115, 2005.



**Hindawi**

Submit your manuscripts at  
[www.hindawi.com](http://www.hindawi.com)

